

Magnetically Guided Synthesis of Anisotropic Porous Carbons toward Efficient CO₂ Capture and Magnetic Separation of Oil

Joelle Medinger, Kyung Seob Song, Pacifique Umubyeyi, Ali Coskun,* and Marco Lattuada*



Read Online

ACCESS |



Metrics & More



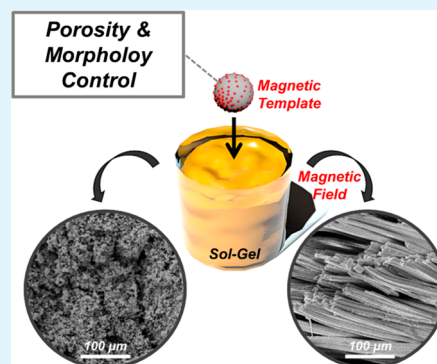
Article Recommendations



Supporting Information

ABSTRACT: Conventional synthetic strategies do not allow one to impart structural anisotropy into porous carbons, thus leading to limited control over their textural properties. While structural anisotropy alters the mechanical properties of materials, it also introduces an additional degree of directionality to increase the pore connectivity and thus the flux in the designed direction. Accordingly, in this work the structure of porous carbons prepared from resorcinol–formaldehyde gels has been rendered anisotropic by integrating superparamagnetic colloids to the sol–gel precursor solution and by applying a uniform magnetic field during the sol–gel transition, which enables the self-assembly of magnetic colloids into chainlike structures to template the growth of the gel phase. Notably, the anisotropic pore structure is maintained upon pyrolysis of the gel, leading to hierarchically porous carbon monoliths with tunable structure and porosities. With an advantage granted to anisotropic materials, these porous carbons showed higher porosity, a higher CO₂ uptake capacity of 3.45 mmol g⁻¹ at 273 K at 1.1 bar, and faster adsorption kinetics compared to the ones synthesized in the absence of magnetic field. Moreover, these materials were also used as magnetic sorbents with fast adsorption kinetics for efficient oil-spill cleanup and retrieved easily by using an external magnetic field.

KEYWORDS: Anisotropic materials, superparamagnetic iron oxide nanocrystals, carbon xerogels, porous carbon, oil capture, gas capture



1. INTRODUCTION

Porous carbons have been investigated extensively in numerous applications, such as gas separation, water remediation, heterogeneous catalysis, and energy storage, because of their good physical and chemical stability, high surface areas, hierarchical porosity, electrical conductivity, and easy functionalization for the incorporation of various heteroatoms.^{1–7} Porous carbons are amorphous networks with rather complex structures, and they can be simply produced via pyrolysis of either biomass or porous organic gels formed through chemical synthesis.^{4,8–10} These synthetic strategies, however, provide limited control over the structure and porosity of the synthetic carbons, thus leading to a significant variation in terms of structure, heteroatom content, and porosity. The incorporation of various templates has also been investigated to control the textural properties of porous carbons.¹¹ Whereas metal–organic framework (MOF)-derived porous carbons have drawn great interest because they inherit the high surface area and structural tunability of MOFs, they still present significant drawbacks such as micropore-dominated structures, irreversible agglomeration of metal nanoparticles, and limited control over structure evolution during carbonization.¹² Furthermore, MOFs are currently still very expensive.

Sol–gel-processed organic gels can be tuned in situ to control the onset of phase separation against gelation of the

sol.^{13–18} In this direction, resorcinol–formaldehyde (RF) gels, originally produced by Pekala,¹⁹ became the first organic aerogels prepared by sol–gel polycondensation.^{20–23} The tunability of the sol–gel process to control the properties of the resulting gels offers a promising strategy to produce gel-derived porous carbon materials. In the sol–gel process, the liquid precursor typically undergoes two types of reactions: hydrolysis and condensation. All changes in the relative rates of these two steps have a profound influence on the final porous structure of the RF gel.^{8,24,25} The porosity is maintained when the organic gels are carbonized into carbon. The introduction of structural anisotropy into porous carbons offers several advantages,^{26–30} which are (1) hierarchical porosity for efficient mass transport, in particular, for catalytic applications, (2) directionality of the pore scaffold and improved pore connectivity, and (3) increased mechanical resistance.^{31–33} In the case of aligned pores, for example, an increased flux control or enhanced uptake of liquid or gas in the direction of pores can be achieved.³⁴ Anisotropic structures and high structural

Received: March 9, 2023

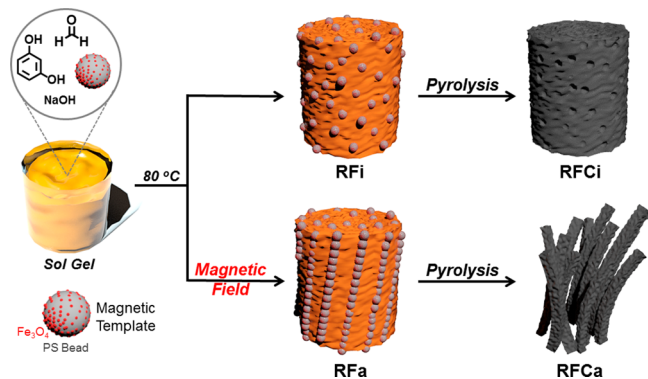
Accepted: April 5, 2023

Published: April 20, 2023

control can be found abundantly in natural systems, such as in mollusk shells, in arthropods such as crabs, or in teeth and bones, to increase the mechanical resistance.^{35–37} While nature has perfected its control over the structure of complex natural materials, precise control over the architecture of artificial or synthetic materials is still highly limited yet highly desired.

While many templating routes exist to tune the porosity of porous carbons, it is much harder to introduce directionality or anisotropy into these materials.^{38–42} In many cases, while the use of templates provides control over the pore structure of porous carbons, removal of the template poses problems due to possible pore or structure collapse or changes in the surface properties of the material. Putz and co-workers²⁷ have achieved anisotropy in the morphology of their carbon material by using nanocasting together with a hard template or using a soft-templating approach by compressing a flexible gel during the carbonization process.²⁷ In these examples, the morphology of the carbon was altered, but the directionality could not have been introduced in the porous carbons. The use of magnetic particles to introduce anisotropy in the structure of a material has been investigated and has the additional advantage of making the material magnetically responsive.^{43–46} In this direction, Lattuada et al.⁴⁷ and Studart et al.^{43,48} have used superparamagnetic colloids as a hard template to introduce a fiber-like or platelet structures into sol–gel-processed silica monoliths.^{29,47,49,50} The development of anisotropic porous carbons with direction-dependent properties, on the other hand, has yet to be realized. In this direction, herein, we demonstrate, for the first time (Scheme 1), a single-step approach to produce magnetically guided

Scheme 1. Preparation of Magnetically Responsive Anisotropic (RFCa) and Isotropic (RFCi) Porous Carbons through Pyrolysis of the Magnetically Responsive Rf Xerogels, Which Were Synthesized with (RFa) or without (RFi) a Magnetic Field^a



^aDue to magnetic template alignment, the pore structure and morphology can be tuned.

anisotropic RF xerogels, which are pyrolyzed to yield porous carbons, showing not only anisotropic morphology with a combination of micro- and macropores but also good pore directionality and connectivity. The application of anisotropic porous carbons for both CO₂ capture and oil recovery, followed by magnetic recuperation, showcases the presence of direction-dependent properties arising from anisotropic structure.

2. EXPERIMENTAL SECTION

Materials. FeCl₃ hexahydrate, FeCl₂ dihydrate, 2,2'-azobis(2-methylpropionitrile) (AIBN), dibenzoyl peroxide, styrene, divinylbenzene (DVB), *n*-hexadecane, 3-(methoxysilyl)propyl methacrylate (98%), butyl acrylate, methyl methacrylate, polybutadiene ($M_w = 1500$), ammonia (25%), acetone, ethanol, diethyl ether (Et₂O), sodium dodecyl sulfate (SDS), and acetic acid were purchased from Sigma-Aldrich. Poly(ethylene glycol) ($M_w = 10000$) and *N,N'*-dimethylaniline were obtained from Merck, while ricinoleic acid (RA) and tetramethyl orthosilicate (98%) were purchased from ABCR GmbH.

Resorcinol (99%) and formaldehyde (37 wt % in water, stabilized by 10–12 wt % methanol) were purchased from Sigma-Aldrich, and NaOH for pH adaptation was obtained from Merck. Pump oil, *N*-methyl-2-pyrrolidone (NMP), ethylene glycol (EG), toluene, chloroform, and tetrahydrofuran (THF) were purchased from Sigma-Aldrich. All chemicals were used directly without any further purification.

Magnetite Synthesis. A total of 3.90 g of FeCl₂ dihydrate and 10.70 g of FeCl₃ hexahydrate were added to 180 mL of stripped water (stripping was achieved by bubbling N₂ in water for 30 min). The solution was stirred at 700 rpm until complete dissolution of the iron salts.

A total of 8.54 g of RA and 4.87 g of acetone were mixed and added to the reaction mixture. The mixture was stirred at 1000 rpm and heated to 80 °C. Finally, 27 mL of NH₃ (25%) was added quickly, and the solution was stirred and heated for another 30 min. The mixture was cooled at room temperature at 500 rpm.

The obtained black precipitates were emptied into crystallizers of 150 mL and washed via magnetic decantation. The first washing step was performed with 100 mL of a solution prepared of 500 mL of acetone and 5 mL of RA. Then, the precipitates were further washed three times using 50 mL of deionized water and 100 mL of the same previously prepared RA/acetone solution. Finally, one last washing step was performed with 100 mL of the acetone/RA washing solution, and the precipitates were sonicated for a few minutes before magnetic decantation. After the solvent was removed, the crystallizer was closed with parafilm, and the black precipitates were dried at room temperature for 24 h.

The magnetite nanoparticles were magnetically filtered to get rid of large clusters. A small plastic or glass column was filled with steel wool and placed between the poles of two magnets. The wool was washed twice with Et₂O. Magnetite nanocrystals were dispersed in Et₂O, and the solution was run through the column. Large clusters were retained due to their higher magnetization, while single-crystal particles were able to pass through the column. Finally, Et₂O was removed under high vacuum.

Miniemulsion Polymerization. Magnetic colloids were prepared by miniemulsion polymerization. The oily phase was prepared by mixing 0.147 g of AIBN, 0.12 g of *n*-hexadecane, 0.60 g of DVB, and 5.50 g of styrene. A total of 3 g of magnetite nanocrystals, prepared as previously described, was added to the oil phase, which was then placed in a refrigerator at 4 °C. The water phase was prepared with 0.25 g of SDS and 48 g of water (stripped with N₂). After SDS was dissolved in the aqueous phase, 2 mL of the aqueous phase was removed. The oil phase was then mixed with the water phase under magnetic stirring. The bottle was placed in an ice bath. The mixture was sonicated with a horn sonicator for 30 min (0.5 s, 70% amplitude). The remaining 2 mL of the water phase was added, and the mixture was transferred to a three-neck round-bottomed flask, equipped with a condenser, a mechanical stirrer at 500 rpm, and a septum. The flask was flushed for 5 min with N₂. Finally, the reaction mixture was heated to 70 °C, and the polymerization reaction was carried out for 3–4 h, until monomer conversion reached at least 98%.

Preparation of the RF Xerogel. First, resorcinol was dissolved in the right amount of deionized water. Then, formaldehyde was added to the mixture with respect to a fixed molar ratio of R/F = 0.5. The dilution ratio ($D = \text{total solvent/reactant molar ratio}$) was varied

between $D = 2$ and 10 to study its influence on the morphology of the xerogel. It is important to mention that the dilution ratio refers to the amount of added deionized water as well as the water and methanol contained in the formaldehyde when considering the “total solvent”. “Reactants” refers to the amount of resorcinol and formaldehyde. The pH was adjusted to 5.8 for low pH and 6.5 for high pH by adding proper quantities of a 1 M NaOH solution. For a typical $D = 10$ precursor solution, 17.34 g of resorcinol was dissolved in 67.8 g of deionized water and 23.63 g of formaldehyde solution at 37 wt % was added. Once the pH was adjusted, the reaction mixture was added to a glass vial and put in an oven at 80 °C for at least 4 h until gelation was visually completed. The wet gel was allowed to age for 48 h, followed by solvent exchange with ethanol for 24 h. The ethanol was allowed to evaporate, and the gel was dried at room temperature for 4 days. Finally, the gel was dried under vacuum for 12 h at 60 °C. When magnetic nanoparticles were added to the precursor solution in the form of a miniemulsion, the amount of added water needed to be adjusted by considering the amount of water added with the particles. If a volume percentage of miniemulsion equal to 45 vol % with a 13 wt % solid content was added, corresponding to a concentration of 5.86 wt % of magnetic colloids, the amount of deionized water for a $D = 10$ precursor solution was lowered to 33.5 g. The procedure followed for the formation of a gel was the same as that for the gels prepared without magnetic particles, except that the reaction mixture was placed between two strong permanent magnets during gelation. The application of a uniform field with an electromagnet could not be performed inside an oven. Therefore, a special mold was designed and connected to a thermostatic bath with a pump. Oil was heated at 75 °C and pumped through a tubular system, which heated the mold containing the vial with the RF gel precursor solution. The mold was fixed between the poles of the electromagnet, and the magnetic field could be applied until gelation was completed.

Pyrolysis. Carbonization of the dried xerogels was performed in a Carbolite tube furnace (capable of a maximal temperature of 1200 °C and equipped with a glass tube), under an inert atmosphere using argon at temperatures ranging from 800 °C to 1200 °C, for 1 h, with a heating rate of 10 °C/min.

Oil Capture Test. A mixture of 0.5 mL of all solvents and 5 mL of water was prepared. A pellet-shaped magnetic responsive isotropic porous carbon (RFCi) [or responsive anisotropic porous carbon (RFCa), 13.65 mm × 5.58 mm] was added. The adsorption efficiency was calculated with the following equation: adsorption efficiency (%) = $(g_a - g_b)/g_b$, wherein g_a and g_b are the weights of RFCs before and after oil absorption, respectively. For kinetic study, 50 mg of RFCi (or RFCa) was placed in a graduated cylinder filled with 4 mL of toluene, and then the absorption amount was measured at each required time.

Characterization. Scanning electron microscopy (SEM) images were recorded with the help of a TESCAN Mira 3 LM field emission machine, and transmission electron microscopy (TEM) was performed on a FEI Tecnai Spirit field-emission microscope. A Mettler Toledo TGA 2 sample robot was used to determine the weight percentage of iron particles contained in a carbon xerogel. The crystallinity of the carbon gels was measured with the help of a STADIP powder diffractometer (Cu $K\alpha_1$ radiation), combined with a focused Cu $K\alpha_1$ incident beam from a germanium monochromator with a Mythen1K detector (CCD). The *Diamond* software database was used for peak fitting. Raman measurements were performed on a WITec alpha300 R microscope at a wavelength of 523 nm. For mechanical compression tests, stress–strain curves were recorded using a Zwick/Roell Z010 testing machine equipped with a compression cell of 10 kN.

Brunauer–Emmett–Teller (BET) analysis was conducted using N_2 adsorption and desorption isotherms, which were measured at 77 K on a Micromeritics 3Flex surface characterization analyzer. All samples were degassed at 100 °C for 16 h prior to the analysis. The specific surface areas of the samples were calculated using the BET and Langmuir models in the pressure range where the term $V(1 - P/P_0)$ continuously increases with P/P_0 in the Rouquerol plot. The pore-size distributions of the samples were calculated from N_2 isotherms according to nonlocal density functional theory (NLDFT) with a

nitrogen-based heterogeneous surface mode and the Barrett–Joyner–Halenda (BJH) method with a Harkins and Jura thickness curve. The low-pressure CO_2 adsorption isotherms and CO_2 adsorption kinetic study of the samples were taken on a Micromeritics 3Flex instrument at three different temperatures of 273, 298, and 323 K. The circulator was used to keep the temperature constant during adsorption/desorption analysis. Isothermic heat of absorption (Q_{st}) values were calculated using the standard calculation routine, that is, the Clausius–Clapeyron equation, in *Mathematica*.

CO_2 Adsorption Kinetic Study of RFCi and RFCa. The CO_2 adsorption amount versus time data was collected using a 3Flex (Micromeritics) instrument during CO_2 adsorption measurement up to 1.1 bar at 298 K. The CO_2 adsorption data of RFCi and RFCa were fitted with the first-order model. The assumption is that the adsorption rate is proportional to the amount of CO_2 adsorption at the same limited time. The rate expression equation is

$$Q_{ad} = kx + a \quad (1)$$

where Q_{ad} (mmol g^{-1}) is the CO_2 adsorption amount, k (mmol $g^{-1} \text{ min}^{-1}$) is the first-order rate constant, x is the time (min), and a is the y intercept.

3. RESULTS AND DISCUSSION

In order to promote the formation of anisotropic structures, a superparamagnetic template in the form of magnetic colloids, which were prepared by a miniemulsion polymerization, was used. The superparamagnetic iron oxide nanocrystals were prepared via a modified coprecipitation method, originally proposed by Massart.⁵¹ This method leads to nanocrystals with a relatively large polydispersity and an average diameter of about 10 nm.⁵² A miniemulsion polymerization step was performed to trap these magnetic nanocrystals inside polystyrene beads with a final size of 150 nm (Figure S1A).⁵² This procedure allowed one to conserve the superparamagnetic properties of the single magnetite nanocrystals, but being enclosed inside larger particles increased their overall magnetic moment and their response to magnetic fields. This process also facilitated their handling because these colloids have much better colloidal stability than the original nanocrystals. Magnetic colloids were homogeneously mixed with a liquid precursor solution prior to the application of a uniform external magnetic field during the condensation reaction. These structurally controlled gels showed long fiber-like structures aligned in the direction of the applied field, with loose lateral connections, as opposed to a random fractal structure obtained in the absence of a field.⁴⁹ After gelation, the template stays well dispersed throughout the material. The porosity of RF gels and xerogels can be controlled via the pH (quantity of added catalyst), the type of catalyst, and the dilution factor (water-to-resorcinol ratio).^{24,53–56} The ideal conditions were chosen to be a pH of 5.8, a R/C (resorcinol-to-catalyst molar ratio) of 1000, achieved using NaOH, and a high dilution ratio of 10 to yield highly mesoporous-to-macroporous RF xerogels (Figures S1–S3). A 2-day aging step and solvent exchange were performed on the gels before they were dried in an ambient atmosphere to give the final xerogels. Due to the capillary forces generated by the evaporation of water during the drying step, a proper solvent exchange for optimized drying conditions is crucial to avoid extensive shrinkage and collapse of the porous structure.^{14,17,53} Accordingly, water was first exchanged with ethanol, followed by a second solvent exchange with Et_2O with a lower surface tension, before the gels were dried at room temperature.

Superparamagnetic nanoparticles develop dipole–dipole interactions when exposed to a magnetic field.⁵⁰ These directional dipole–dipole interactions are the strongest when the dipoles are aligned along the direction of the applied field. This promotes self-assembly of the particles into linear chains aligned in the direction of the applied field. Strong magnetic fields of at least 0.5 T were found to be necessary to guarantee a uniform field over the entire length of the RF specimen and to ensure structural control via superparamagnetic templates. At low magnetic fields, field gradients will cause concentration gradients of the template inside the sample up to the point that structural control will fail. In addition to a uniform field, stabilization of the magnetic template is also crucial, so that the templates stay well dispersed inside the precursor solution in order to control the structure of the RF gels. In this direction, SDS was found to be the ideal surfactant to form negatively charged particles and to guarantee good colloidal stability and dispersion of the magnetic particles (Figure S1A) at the low pH values of the RF sol–gel synthesis. Using SDS-stabilized magnetic colloids (6 wt %) and by applying an external magnetic field during gelation, it was possible to obtain RF monoliths with fiber-like, permanently fixed structures, which was verified by the SEM analysis (Figure 1D). The

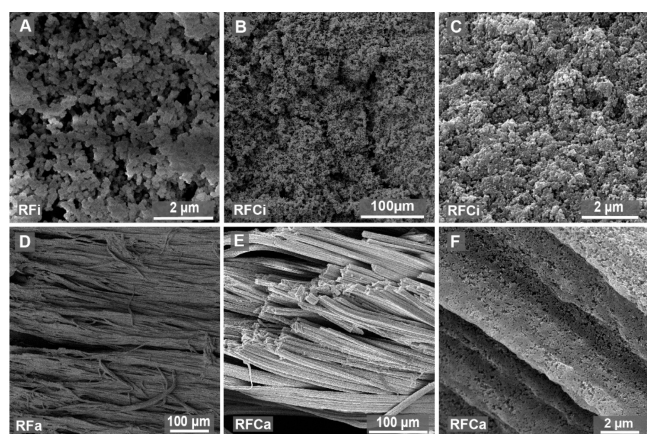


Figure 1. SEM images of isotropic and anisotropic RF xerogels containing magnetic colloids and their pyrolyzed counterparts. (A) RFi with a dilution ratio of 10 and pH 5.8. (B and C) RFCi pyrolyzed at 1000 °C. The porous structure was preserved but isotropic. (D) RFa xerogel with an anisotropic structure at a dilution ratio of 10 and pH 5.8. The fiber-like structure was obtained by the application of an external magnetic field during the condensation reaction to obtain the gel. (E and F) RFCa pyrolyzed at 1000 °C. The anisotropic structure was preserved upon pyrolysis.

morphology of the gels in the absence of an external magnetic field remained random and isotropic (Figure 1A).¹⁵ Notably, the chemical structure of the RF gels is not altered by the presence of the magnetic template, which was verified by the preparation of monoliths outside a magnetic field with or without added magnetic colloids in the RF precursor solution (Figure S4). RF xerogels containing a magnetic template were referred to as RFi when they had an *isotropic* structure and RFa when they had an *anisotropic* structure. The successful preparation of RF xerogels containing magnetic colloids was followed by a pyrolysis step (parts B,C and E,F of Figure 1). Pyrolysis of the RF gels was performed at temperatures ranging from 800 to 1200 °C for 2 h at a 10 °C/min heating rate under an argon atmosphere.

The resulting porous carbons were named RFCa and RFCi for the anisotropic and isotropic samples, respectively. With the help of powder X-ray diffraction (XRD) analysis (Figures S5 and S6A), we observed not only a broad band at $2\theta = 25^\circ$, which is attributed to π – π stacking between the graphitic layers, but also a reduction in the d spacing (development of the microstructure) of the carbon structure with increasing temperature from 800 to 1000 °C. Above 1000 °C, the magnetic template was completely reduced to metallic iron, and at 1200 °C, the oxide peaks of iron oxide had completely disappeared and the metallic iron peak was clearly visible. The iron content inside the porous carbons, RFCa and RFCi, was determined by thermogravimetric analysis (TGA). When no magnetic template was added during the gel synthesis, the weight loss was 100%. The precursor solution with 6 wt % magnetic template, on the other hand, showed 14 wt % metallic iron after carbonization (Figures S7 and S8). In order to maximize development of the microstructure while preserving the presence of magnetite for its superparamagnetic properties, a pyrolysis temperature of 1000 °C was chosen as the optimum. All further characterizations were performed using porous carbons pyrolyzed at 1000 °C. We performed Raman spectroscopy analysis, and the obtained spectra show two vibrational peaks characteristic of the graphitic structure (Figure S6B). The D peak at 1350 cm^{-1} (A_{1g}) showed the disordered graphitic carbon structure, while the peak at 1562 cm^{-1} was assigned to the graphitic vibrational mode of the sp^2 -hybridized carbons, which is the G peak (E_{2g}). The multilayer graphitic structure was confirmed by the I_D/I_G ratio of 0.86.⁵⁷ Notably, the rod-like structure of the RF gels was preserved during pyrolysis (Figure 1E,F). We also performed energy-dispersive X-ray (EDX) mapping analysis of porous carbons to characterize their structure and dispersion of the template in the material. The elemental mapping results confirmed the anisotropic structure of the material and with homogeneous dispersion of iron in RFCa (Figure 2, bottom), whereas an isotropic structure was observed for RFCi (Figure 2, top).

To analyze the impact of the anisotropic carbon structure on the mechanical properties of the material, the stress–strain curve of a set of fiber-structured porous carbons was measured and the results were compared to Young’s modulus (E_c) measured for the isotropic porous carbons (Figures S9 and S10). In the case of isotropic porous carbons, Young’s modulus was independent of the orientation and varied therefore only very little from the parallel to perpendicular orientation. The isotropic porous carbon samples showed the average Young’s modulus varying between 11.5 MPa (parallel) and 14 MPa (perpendicular). Notably, porous carbons with anisotropic structure presented exceptional mechanical strength when compressed in the direction of the controlled structure (parallel) with 17.3 MPa, while they were found to be mechanically weaker in the perpendicular direction (perpendicular) with an average Young’s modulus of 7.6 MPa.

In order to investigate the textural properties of RFCi and RFCa, we measured N_2 adsorption and desorption isotherms at 77 K (Figure 3A,D). RFCi and RFCa showed type IV isotherms with a H4 hysteresis loop. It is known that evaporation of the capillary condensate from the network was limited by the ink-bottle effect. Thus, desorption from the pore body depends on the size of the neck and the pore connectivity. The fact that RFCa showed a smaller hysteresis loop compared to that of RFCi indicates a much improved pore connectivity in the case of an anisotropic structure. The

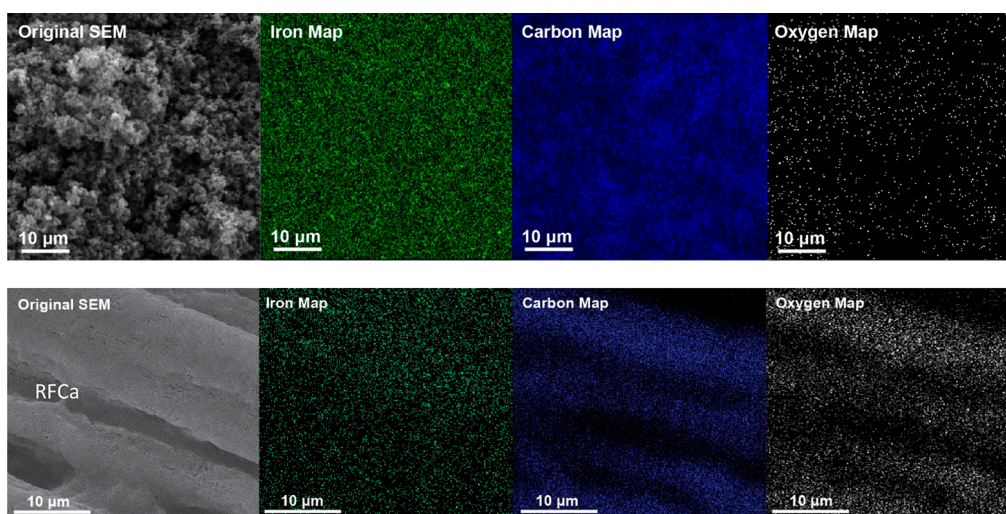


Figure 2. EDX elemental mapping images of iron, carbon, and oxygen for isotropic RFCi (top) and structurally controlled anisotropic RFCa (bottom) samples. The iron mapping images clearly show that iron was well dispersed within the carbon materials. The element mappings of carbon and oxygen, on the other hand, verified the anisotropic structure of RFCa.

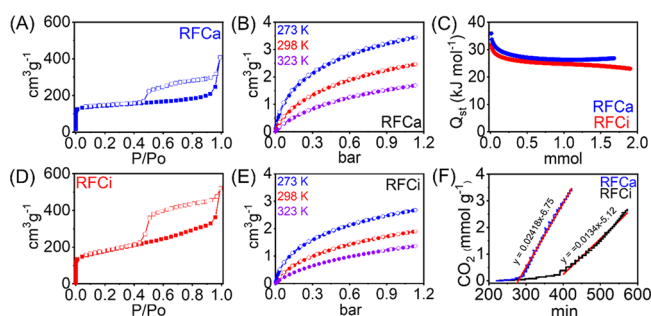


Figure 3. N_2 adsorption–desorption isotherms of (A) RFCa and (D) RFCi recorded at 77 K. CO_2 uptake isotherms of (B) RFCa and (E) RFCi measured at 273, 298, and 323 K up to 1.1 bar. (C) Plots of Q_{st} of CO_2 versus CO_2 amount for RFCa (blue) and RFCi (red). (F) Kinetics of CO_2 adsorption in RFCa and RFCi.

surface areas of RFCa and RFCi were calculated based on the BET model with valid pressure ranges obtained from the Rouquerol plots (Figures S11 and S12). RFCi and RFCa exhibited (Table 1) surface areas of 628 and 550 $m^2 g^{-1}$ and total pore volumes of 0.81 and 0.63 $cm^3 g^{-1}$, respectively. Whereas RFCa showed higher micropore surface area and micropore volume, RFCi was found to be predominantly mesoporous, an effect that can only be explained by magnetically guided structure and porosity control because both RFCi and RFCa have otherwise identical chemical composition.

These results suggest that the self-assembly of the magnetic template into linear chains clearly improves the pore connectivity and pore accessibility for RFCa. The NLDFT

and BJH models were used to determine the pore size and pore-size distribution of RFCi and RFCa. The NLDFT pore-size distribution of RFCa showed three pore maxima of 0.44, 0.59, and 0.99 nm, whereas RFCi showed two maxima of 0.53 and 0.9 nm (Figures S12 and S13). In the BJH analysis, RFCa and RFCi showed mesoporous structure (up to 20 nm; Figure S14).

In order to probe the effect of magnetically guided structure control on the gas uptake properties of RFCa and RFCi, we measured CO_2 adsorption isotherms at 273, 298, and 323 K up to 1.1 bar (Figure 3B,E). Whereas RFCi showed a CO_2 uptake capacity of 2.67 $mmol g^{-1}$ at 1.1 bar, RFCa showed 3.45 $mmol g^{-1}$ of CO_2 uptake at 1.1 bar. The higher CO_2 uptake capacity of RFCa was attributed to the higher micropore surface area of RFCa compared to RFCi. The Q_{st} value calculated by the Clausius–Clapeyron equation showed 35.88 and 31.64 $kJ mol^{-1}$ for RFCa and RFCi at zero coverage, respectively (Table 1 and Figure 3C). This significant difference is attributed to the combined effect of the high micropore surface area, the presence of ultramicropores, and the improved accessibility of these pores in the case of RFCa.⁵⁸ In order to probe the impact of the anisotropic structure of RFCa with aligned pores on the mass-transport kinetics, we compared the CO_2 adsorption kinetics of RFCa and RFCi (Figure 3F) at 273 K. To investigate CO_2 adsorption kinetics, we used the interpolation method to fit the adsorption graphs. Notably, CO_2 molecules were adsorbed much faster in RFCa (0.02418 $mmol g^{-1} min^{-1}$) compared to RFCi (0.0134 $mmol g^{-1} min^{-1}$), which was attributed to the improved pore connectivity in RFCa enabling efficient mass transport. These findings clearly demonstrate the profound impact of porosity control with a

Table 1. Surface Area Analysis of RFCi and RFCa with CO_2 Capture

sample name	S_{BET}^a [$m^2 g^{-1}$]	Langmuir [$m^2 g^{-1}$]	S_{micro}^b [$m^2 g^{-1}$]	S_{ext}^c [$m^2 g^{-1}$]	V_{total}^c [$cm^3 g^{-1}$]	V_{micro}^d [$cm^3 g^{-1}$]	CO_2 uptake			
							273 K	298 K	322 K	$kJ mol^{-1}$
RFCi	628	776	244	384	0.81	0.10	3.45	2.46	1.68	35.88
RFCa	550	628	397	153	0.63	0.16	2.67	1.90	1.36	31.64

^aBET surface area calculated over the pressure range (P/P_0). ^bMicropore surface area calculated from the adsorption isotherm using the t-plot method. ^cTotal pore volume obtained at $P/P_0 = 0.99$. ^dMicropore volume calculated using the t-plot method.

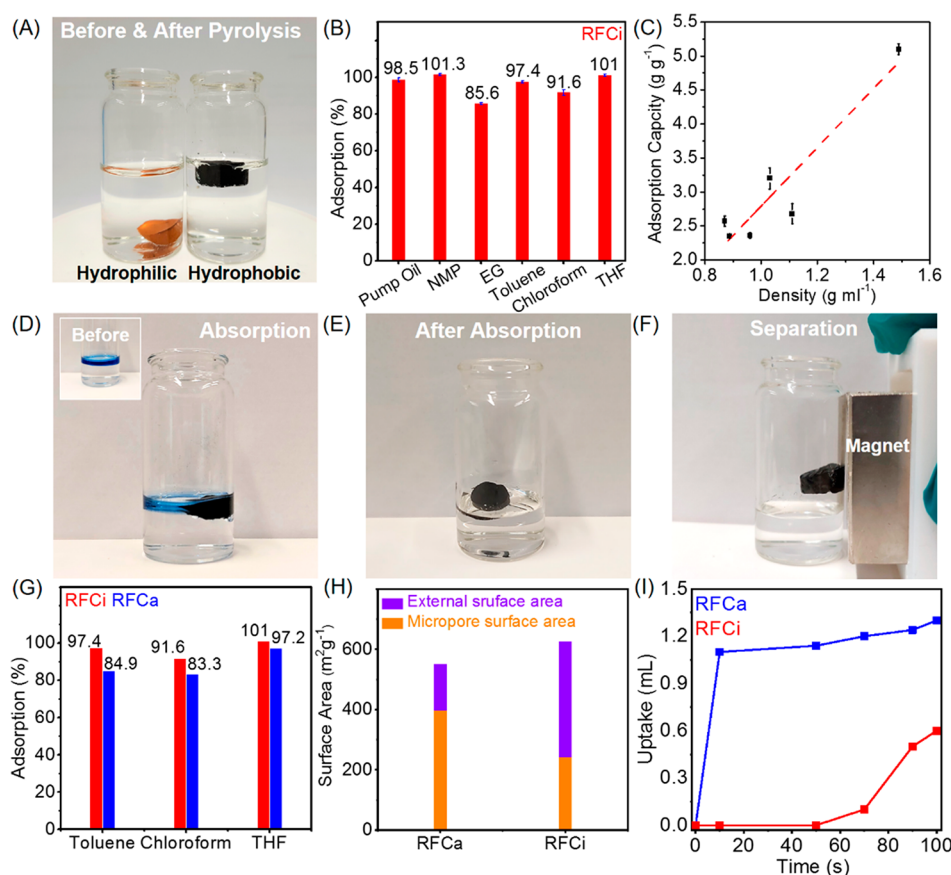


Figure 4. Selective oil capture from the oil/water mixture. (A) Physical property changes of RF xerogels before and after pyrolysis. (B) Oil and organic solvent capture test of RFCi. (C) Relationship between the solvent density and absorption capacity of RFCi. (D) RFCi absorption of dark-blue toluene from water. (E) After absorption of RFCi. (F) Magnetic separation of RFCi. (G) Absorption capacity comparison of RFCi and RFCa. (H) Surface area composition of RFCa and RFCi. A higher external surface area shows a higher absorption capacity. (I) Absorption kinetics study of RFCi and RFCa using toluene. The diameter of the glass vials shown in parts A and D–F is roughly 2 cm.

magnetic template on the surface area, CO₂ uptake capacity, and adsorption kinetics.

We also investigated the performance of RFCs in oil capture due to their high porosity, hydrophobic character, and magnetic responsiveness, which enables easy retrieval using an extremal magnetic field. Oil spills in the ocean or fresh water sources have major, long-lasting impacts on the marine ecosystem and coastal environment.^{59,60} Therefore, it is essential to develop environmentally friendly and low-cost solid sorbents that can be easily recovered following oil uptake.^{60–67} The incorporation of magnetic nanoparticles in porous materials has been actively investigated for environmental remediation.^{4,63–65,67} However, most of these approaches involve rather elaborate, multistep syntheses to render the materials magnetic. In this sense, our approach to preparing RFCs presents significant advantages due to the ease of their synthesis, efficient mass transport, and improved kinetics, along with a high and well-dispersed iron content.

In order to probe the hydrophilicity/hydrophobicity of the polymer and porous carbons, we added RFi and RFCi to water (Figure 4A). Whereas the RFi gel sank into the water due to the hydrophilicity of the surface hydroxyl groups, RFCi floated due to its hydrophobic surface. To further test the RFCi oil capture ability, pump oil and organic solvents (NMP, EG, toluene, chloroform, and THF) were also tested (Figure 4B). RFCi showed 85.5–100% absorption efficiency (calculated by the weight change of RFCi before and after the absorption test,

as shown in the experimental part). Depending on the solvent density, the RFCi absorption capacity (oil and organic solvents) was determined and showed a linear relationship between the adsorption capacity and solvent density (Figure 4C). In order to investigate the oil capture performance of RFCs, a mixture of toluene and water was prepared in a vial. To visually distinguish toluene from water, a dark-blue organic ink was added to the toluene phase (Figure 4D). The colored toluene phase was completely absorbed by RFCi with vigorous bubbling (Figure 4E). A permanent magnet was then used to easily recover RFCi from the liquid (Figure 4F). Moreover, we also measured the RFCa oil absorption capacity and compared it to that of RFCi (Figure 4G). RFCi showed higher absorption capacities than RFCa due to its higher external surface area (Figure 4H). A comparison of the absorption kinetics using toluene (Figure 4I), on the other hand, revealed much faster absorption kinetics for RFCa compared to RFCi, thus proving the critical role of an anisotropic structure and aligned pores for enhanced mass-transport kinetics (Figure 3F). Recovery of the organic liquid from RFCs was possible with distillation rather than by squeezing of the sample due to its rigidity.^{63,67} RFCs can be reused after vacuum evaporation of the solvent.^{4,64} From an industrial perspective, one can easily produce RFCs in pellet form, with varying shape and thickness, depending on the mold used for the sol-gel precursor.

4. CONCLUSIONS

In this work, we showed for the first time a magnetically guided synthesis of anisotropic porous carbons with fiber-like structures through the pyrolysis of RF xerogels containing superparamagnetic colloids. In addition to an enhanced mechanical resistance, the impact of the pore alignment of the anisotropic porous carbons was clearly demonstrated by oil and CO₂ capture experiments, showing substantially improved mass-transport kinetics. As an added advantage, the magnetite nanocrystals remaining inside the carbon materials rendered them highly magnetically responsive. Control of the directionality (anisotropy) of the pores and structure in porous carbons as well as the presence of well-dispersed iron species make these materials very promising for heterogeneous catalysis and energy storage applications. It should be noted that the porosity and CO₂ adsorption capacity of the materials obtained in our work are smaller than those of some of the carbon-based materials reported in the literature, typically by a factor of 2 or 3.^{68,69} This is not surprising because the objective of this work was to optimize the synthesis conditions for optimal magnetic control of the structure, thus tuning their macroporosity so that the formation of RF rods could be optimized. Control of the microporosity was not a primary objective of the work, which explains the smaller porosity compared to those of other works in the literature.^{68,69} It should be noted that the composition of the sol–solution can be tuned so as to increase the meso- and microporosity of the resulting gels and carbon materials, which would however render more difficult the assessment of the pore alignment looked for in this work. Furthermore, some of the methods used in the literature to increase the porosity of the carbon-based materials, such as activation using bases, could be applied to our system as well, leaving space for further improvement in the porosity and adsorption capacity.

There are other methods in the literature that can be used to induce anisotropy in porous materials. Perhaps the most commonly used strategies is directional freeze casting.⁷⁰ This consists of letting ice crystals grow inside an aqueous suspension of a solid precursor. The growth of ice crystals leads to well-aligned macropores, which have been used, for example, to align carbon nanotubes and cellulose nanocrystals, leading to the formation of aerogels upon ice removal. The pores obtained by directional freeze casting possess primarily honeycomb structures, while the pores obtained in our work are the empty spaces left by fibers. Compared to directional freeze casting, our approach has the advantage of directly providing materials with magnetic properties that are ideal for magnetic recovery applications. Control of the magnetic field configuration can furthermore be used to change the structure of the materials completely, as shown in a previous work for the case of silica, where rotating fields were used to create a lamellar structure.²⁹

■ ASSOCIATED CONTENT

SI Supporting Information

The Supporting Information is available free of charge at <https://pubs.acs.org/doi/10.1021/acsami.3c03424>.

Additional SEM and TEM images, XRD, TGA, and BET data, and mechanical properties analysis (PDF)

■ AUTHOR INFORMATION

Corresponding Authors

Ali Coskun – Department of Chemistry, University of Fribourg, 1700 Fribourg, Switzerland; orcid.org/0000-0002-4760-1546; Email: ali.coskun@unifr.ch

Marco Lattuada – Department of Chemistry, University of Fribourg, 1700 Fribourg, Switzerland; orcid.org/0000-0001-7058-9509; Email: marco.lattuada@unifr.ch

Authors

Joelle Medinger – Department of Chemistry, University of Fribourg, 1700 Fribourg, Switzerland

Kyung Seob Song – Department of Chemistry, University of Fribourg, 1700 Fribourg, Switzerland

Pacifique Umubyeyi – Department of Chemistry, University of Fribourg, 1700 Fribourg, Switzerland

Complete contact information is available at:

<https://pubs.acs.org/10.1021/acsami.3c03424>

Author Contributions

J.M., K.S.S., M.L., and A.C. conceived the work. J.M., K.S.S., and P.U. performed the experiments, and J.M. and K.S.S. wrote the manuscript. All the authors edited and commented on the manuscript.

Notes

The authors declare no competing financial interest.

■ ACKNOWLEDGMENTS

M.L. gratefully acknowledges financial support from the University of Fribourg, as well as the NCCR program bioinspired materials. A.C. acknowledges the Swiss National Science Foundation for funding this research (Grant 200021-175947).

■ REFERENCES

- (1) Casco, M. E.; Martínez-Escandell, M.; Silvestre-Albero, J.; Rodríguez-Reinoso, F. Effect of the Porous Structure in Carbon Materials for CO₂ Capture at Atmospheric and High-Pressure. *Carbon N. Y.* **2014**, *67*, 230–235.
- (2) Dai, J.; Zhang, R.; Ge, W.; Xie, A.; Chang, Z.; Tian, S.; Zhou, Z.; Yan, Y. 3D Macroscopic Superhydrophobic Magnetic Porous Carbon Aerogel Converted from Biorenewable Popcorn for Selective Oil-Water Separation. *Mater. Des.* **2018**, *139*, 122–131.
- (3) Gaikwad, M. M.; Kakunuri, M.; Sharma, C. S. Enhanced Catalytic Graphitization of Resorcinol Formaldehyde Derived Carbon Xerogel to Improve Its Anodic Performance for Lithium Ion Battery. *Mater. Today Commun.* **2019**, *20*, 100569.
- (4) Raj, K. G.; Joy, P. A. Coconut Shell Based Activated Carbon-Iron Oxide Magnetic Nanocomposite for Fast and Efficient Removal of Oil Spills. *J. Environ. Chem. Eng.* **2015**, *3* (3), 2068–2075.
- (5) Tian, L.; Ji, D.; Zhang, S.; He, X.; Ramakrishna, S.; Zhang, Q. A Humidity-Induced Nontemplating Route toward Hierarchical Porous Carbon Fiber Hybrid for Efficient Bifunctional Oxygen Catalysis. *Small* **2020**, *16* (23), 2001743.
- (6) Zhao, L. Y.; Dong, X. L.; Lu, A. H. Mechanochemical Synthesis of Porous Carbons and Their Applications in Catalysis. *ChemPlusChem.* **2020**, *85* (5), 866–875.
- (7) Song, M.; Zhou, Y.; Ren, X.; Wan, J.; Du, Y.; Wu, G.; Ma, F. Biowaste-Based Porous Carbon for Supercapacitor: The Influence of Preparation Processes on Structure and Performance. *J. Colloid Interface Sci.* **2019**, *535*, 276–286.
- (8) Antonietti, M.; Fechler, N.; Feller, T.-P. Carbon Aerogels and Monoliths: Control of Porosity and Nanoarchitecture via Sol–Gel Routes. *Chem. Mater.* **2014**, *26*, 196–210.

- (9) Zhou, X. L.; Zhang, H.; Shao, L. M.; Lü, F.; He, P. J. Preparation and Application of Hierarchical Porous Carbon Materials from Waste and Biomass: A Review. *Waste and Biomass Valorization* **2021**, *12* (4), 1699–1724.
- (10) Sophia A, C.; Lima, E. C. Removal of Emerging Contaminants from the Environment by Adsorption. *Ecotoxicol. Environ. Saf.* **2018**, *150*, 1–17.
- (11) Tian, W.; Zhang, H.; Duan, X.; Sun, H.; Shao, G.; Wang, S. Porous Carbons: Structure-Oriented Design and Versatile Applications. *Adv. Funct. Mater.* **2020**, *30* (17), 1909265.
- (12) Wang, C.; Kim, J.; Tang, J.; Kim, M.; Lim, H.; Malgras, V.; You, J.; Xu, Q.; Li, J.; Yamauchi, Y. New Strategies for Novel MOF-Derived Carbon Materials Based on Nanoarchitectures. *Chem.* **2020**, *6* (1), 19–40.
- (13) Yoon, H. J.; Lee, J. Y.; Lee, J. S.; Yoon, T. H. Monolithic Carbon Xerogel with Co-Continuous Hierarchical Porosity via One-Step, Template- and Catalyst-Free Hydrothermal Reaction with Resorcinol and Formaldehyde. *RSC Adv.* **2019**, *9* (17), 9480–9485.
- (14) Al-Muhtaseb, S. A.; Ritter, J. A. Preparation and Properties of Resorcinol-Formaldehyde Organic and Carbon Gels. *Adv. Mater.* **2003**, *15* (2), 101–114.
- (15) Job, N.; Gommès, C. J.; Pirard, R.; Pirard, J. P. Effect of the Counter-Ion of the Basification Agent on the Pore Texture of Organic and Carbon Xerogels. *J. Non. Cryst. Solids* **2008**, *354* (40–41), 4698–4701.
- (16) Tamon, H.; Ishizaka, H.; Araki, T.; Okazaki, M. Control of Mesoporous Structure of Organic and Carbon Aerogels. *Carbon N. Y.* **1998**, *36* (9), 1257–1262.
- (17) Elkhatat, A. M.; Al-Muhtaseb, S. A. Advances in Tailoring Resorcinol-Formaldehyde Organic and Carbon Gels. *Adv. Mater.* **2011**, *23* (26), 2887–2903.
- (18) Nakanishi, K. Functional Porous Materials via Sol-Gel with Phase Separation. *J. Ceram. Soc. Japan* **2007**, *115*, 169–175.
- (19) Pekala, R. W. Organic Aerogels from the Polycondensation of Resorcinol with Formaldehyde. *J. Mater. Sci.* **1989**, *24* (9), 3221–3227.
- (20) Pekala, R. W.; Schaefer, D. W. Structure of Organic Aerogels. I. Morphology and Scaling. *Macromolecules* **1993**, *26* (20), 5487–5493.
- (21) Pekala, R. W.; Alviso, C. T.; Kong, F. M.; Hulse, S. S. Aerogels Derived from Multifunctional Organic Monomers. *J. Non. Cryst. Solids* **1992**, *145* (C), 90–98.
- (22) Pekala, R. W. Synthetic Control of Molecular Structure in Organic Aerogels. *Mater. Res. Soc.* **1989**, *171*, 285–291.
- (23) Tannert, R.; Schwan, M.; Ratke, L. Reduction of Shrinkage and Brittleness for Resorcinol-Formaldehyde Aerogels by Means of a pH-Controlled Sol-Gel Process. *J. Supercrit. Fluids* **2015**, *106*, 57.
- (24) Job, N.; Pirard, R.; Marien, J.; Pirard, J. P. Porous Carbon Xerogels with Texture Tailored by pH Control during Sol-Gel Process. *Carbon N. Y.* **2004**, *42* (3), 619–628.
- (25) Rey-Raap, N.; Angel Menéndez, J.; Arenillas, A. RF Xerogels with Tailored Porosity over the Entire Nanoscale. *Microporous Mesoporous Mater.* **2014**, *195*, 266–275.
- (26) Hasegawa, G.; Kanamori, K.; Kiyomura, T.; Kurata, H.; Abe, T.; Nakanishi, K. Hierarchically Porous Carbon Monoliths Comprising Ordered Mesoporous Nanorod Assemblies for High-Voltage Aqueous Supercapacitors. *Chem. Mater.* **2016**, *28* (11), 3944–3950.
- (27) Putz, F.; Ludescher, L.; Elsaesser, M. S.; Paris, O.; Hüsing, N. Hierarchically Organized and Anisotropic Porous Carbon Monoliths. *Chem. Mater.* **2020**, *32* (9), 3944–3951.
- (28) Geng, S.; Wei, J.; Jonasson, S.; Hedlund, J.; Oksman, K. Multifunctional Carbon Aerogels with Hierarchical Anisotropic Structure Derived from Lignin and Cellulose Nanofibers for CO₂ Capture and Energy Storage. *ACS Appl. Mater. Interfaces* **2020**, *12* (6), 7432–7441.
- (29) Medinger, J.; Nedyalkova, M.; Furlan, M.; Lüthi, T.; Hofmann, J.; Neels, A.; Lattuada, M. Preparation and Machine-Learning Methods of Nacre-like Composites from the Self-Assembly of Magnetic Colloids Exposed to Rotating Magnetic Fields. *ACS Appl. Mater. Interfaces* **2021**, *13* (40), 48040–48052.
- (30) Erb, R. M.; Libanori, R.; Rothfuchs, N.; Studart, A. R. Composites Reinforced in Three Dimensions by Using Low Magnetic Fields. *Science* **2012**, *335* (6065), 199–204.
- (31) Luo, B.; Li, Z.; Zhang, J.; Wang, X. Formation of Anisotropic Microporous Isotactic Polypropylene (IPP) Membrane via Thermally Induced Phase Separation. *Desalination* **2008**, *233* (1–3), 19–31.
- (32) Nickel, A. C.; Scotti, A.; Houston, J. E.; Ito, T.; Crassous, J.; Pedersen, J. S.; Richtering, W. Anisotropic Hollow Microgels That Can Adapt Their Size, Shape, and Softness. *Nano Lett.* **2019**, *19* (11), 8161–8170.
- (33) Ahmed, A.; Joshi, I. M.; Larson, S.; Mansouri, M.; Gholizadeh, S.; Allahyari, Z.; Forouzandeh, F.; Borkholder, D. A.; Gaborski, T. R.; Abhyankar, V. V. Microengineered 3D Collagen Gels with Independently Tunable Fiber Anisotropy and Directionality. *Adv. Mater. Technol.* **2021**, *6* (4), 2001186.
- (34) Restrepo-Flórez, J. M.; Maldovan, M. Anisotropic Membrane Materials for Gas Separations. *AIChE J.* **2019**, *65* (6). DOI: 10.1002/aic.16599
- (35) Meyers, M. A.; Chen, P. Y.; Lin, A. Y. M.; Seki, Y. Biological Materials: Structure and Mechanical Properties. *Prog. Mater. Sci.* **2008**, *53*, 1–206.
- (36) Barthelat, F.; Tang, H.; Zavattieri, P. D.; Li, C. M.; Espinosa, H. D. On the Mechanics of Mother-of-Pearl: A Key Feature in the Material Hierarchical Structure. *J. Mech. Phys. Solids* **2007**, *55* (2), 306–337.
- (37) Studart, A. R. Towards High-Performance Bioinspired Composites. *Adv. Mater.* **2012**, *24* (37), 5024–5044.
- (38) Shahbazi, M. A.; Ghalkhani, M.; Maleki, H. Directional Freeze-Casting: A Bioinspired Method to Assemble Multifunctional Aligned Porous Structures for Advanced Applications. *Adv. Eng. Mater.* **2020**, *22*, 2000033.
- (39) Qian, L.; Zhang, H. Controlled Freezing and Freeze Drying: A Versatile Route for Porous and Micro-/Nano-Structured Materials. *J. Chem. Technol. Biotechnol.* **2011**, *86* (2), 172–184.
- (40) Yang, X.-Y.; Chen, L.-H.; Li, Y.; Rooke, J. C.; Sanchez, C.; Su, B.-L. Hierarchically Porous Materials: Synthesis Strategies and Structure Design. *Chem. Soc. Rev.* **2017**, *46*, 481–558.
- (41) Ibarra Torres, C. E.; Serrano Quezada, T. E.; Kharisova, O. V.; Kharisov, B. I.; Gómez de la Fuente, M. I. Carbon-Based Aerogels and Xerogels: Synthesis, Properties, Oil Sorption Capacities, and DFT Simulations. *J. Environ. Chem. Eng.* **2021**, *9* (1), 104886.
- (42) Tao, G.; Zhang, L.; Hua, Z.; Chen, Y.; Guo, L.; Zhang, J.; Shu, Z.; Gao, J.; Chen, H.; Wu, W.; Liu, Z.; Shi, J. Highly Efficient Adsorbents Based on Hierarchically Macro/Mesoporous Carbon Monoliths with Strong Hydrophobicity. *Carbon N. Y.* **2014**, *66*, 547–559.
- (43) Erb, R. M.; Libanori, R.; Rothfuchs, N.; Studart, A. R. Composites Reinforced in Three Dimensions by Using Low Magnetic Fields. *Science (80-)* **2012**, *335* (6065), 199–204.
- (44) Le Ferrand, H.; Bouville, F.; Niebel, T. P.; Studart, A. R. Magnetically Assisted Slip Casting of Bioinspired Heterogeneous Composites. *Nat. Mater.* **2015**, *14* (11), 1172–1179.
- (45) Heiligtag, F. J.; Airaghi Leccardi, M. J. I.; Erdem, D.; Süess, M. J.; Niederberger, M. Anisotropically Structured Magnetic Aerogel Monoliths. *Nanoscale* **2014**, *6* (21), 13213–13221.
- (46) Leventis, N.; Elder, I. A.; Long, G. J.; Rolison, D. R. Using Nanoscopic Hosts, Magnetic Guests, and Field Alignment to Create Anisotropic Composite Gels and Aerogels. *Nano Lett.* **2002**, *2* (1), 63–67.
- (47) Furlan, M.; Lattuada, M. Fabrication of Anisotropic Porous Silica Monoliths by Means of Magnetically Controlled Phase Separation in Sol–Gel Processes. *Langmuir* **2012**, *28* (34), 12655–12662.
- (48) Grossman, M.; Erni, F.; Bouville, F.; Libanori, R.; Studart, A. R. Bioinspired Composites by Vacuum Assisted Magnetic Alignment. *ECCM 2016: Proceedings of the 17th European Conference on Composite Materials; European Conference on Composite Materials (ECCM)*, 2016.

- (49) Furlan, M.; Brand, B.; Lattuada, M. Magnetic Gelation: A New Method for the Preparation of Polymeric Anisotropic Porous Materials. *Soft Matter* **2010**, *6* (21), 5636–5644.
- (50) Lattuada, M.; Furlan, M.; Harshe, Y. Field-Controlled Self-Assembly and Disassembly of Colloidal Nanoparticles. *Chim. Int. J. Chem.* **2011**, *65* (10), 792–798.
- (51) Massart, R. Preparation of Aqueous Magnetic Liquids in Alkaline and Acidic Media. *IEEE Trans. Magn.* **1981**, *17* (2), 1247–1248.
- (52) Ramírez, L. P.; Landfester, K. Magnetic Polystyrene Nanoparticles with a High Magnetite Content Obtained by Miniemulsion Processes. *Macromol. Chem. Phys.* **2003**, *204* (1), 22–31.
- (53) Czakkel, O.; Marthi, K.; Geissler, E.; László, K. Influence of Drying on the Morphology of Resorcinol-Formaldehyde-Based Carbon Gels. *Microporous Mesoporous Mater.* **2005**, *86* (1–3), 124–133.
- (54) Rey-Raap, N.; Arenillas, A.; Menéndez, J. A. A Visual Validation of the Combined Effect of PH and Dilution on the Porosity of Carbon Xerogels. *Microporous Mesoporous Mater.* **2016**, *223*, 89.
- (55) Kinnertová, E.; Slovák, V. Influence of Catalyst Amount on Properties of Resorcinol-Formaldehyde Xerogels. *Thermochim. Acta* **2018**, *660*, 37–43.
- (56) Calvo, E. G.; Menéndez, J. A.; Arenillas, A. Influence of Alkaline Compounds on the Porosity of Resorcinol-Formaldehyde Xerogels. *J. Non. Cryst. Solids* **2016**, *452*, 286–290.
- (57) Nguyen, V. T.; Le, H. D.; Nguyen, V. C.; Tam Ngo, T. T.; Le, D. Q.; Nguyen, X. N.; Phan, N. M. Synthesis of Multi-Layer Graphene Films on Copper Tape by Atmospheric Pressure Chemical Vapor Deposition Method. *Adv. Nat. Sci. Nanosci. Nanotechnol.* **2013**, *4* (3), 035012.
- (58) Cychoz, K. A.; Guillet-Nicolas, R.; García-Martínez, J.; Thommes, M. Recent Advances in the Textural Characterization of Hierarchically Structured Nanoporous Materials. *Chem. Soc. Rev.* **2017**, *46* (2), 389–414.
- (59) Pavlatou, E. A. Commercial Sponges as a Novel Technology for Crude Oil Removal from Seawater and Industrial Wastewater: A Review. *Biomed. J. Sci. Technol. Res.* **2020**, *25* (5). DOI: 10.26717/BJSTR.2020.25.004251
- (60) Zhang, Y. Q.; Yang, X. B.; Wang, Z. X.; Long, J.; Shao, L. Designing Multifunctional 3D Magnetic Foam for Effective Insoluble Oil Separation and Rapid Selective Dye Removal for Use in Wastewater Remediation. *J. Mater. Chem. A* **2017**, *5* (16), 7316–7325.
- (61) Zhang, T.; Li, Z.; Lü, Y.; Liu, Y.; Yang, D.; Li, Q.; Qiu, F. Recent Progress and Future Prospects of Oil-Absorbing Materials. *Chin. J. Chem. Eng.* **2019**, *27* (6), 1282–1295.
- (62) Guselnikova, O.; Barras, A.; Addad, A.; Sviridova, E.; Szunerits, S.; Postnikov, P.; Boukherroub, R. Magnetic Polyurethane Sponge for Efficient Oil Adsorption and Separation of Oil from Oil-in-Water Emulsions. *Sep. Purif. Technol.* **2020**, *240*, 116627.
- (63) Wu, L.; Li, L.; Li, B.; Zhang, J.; Wang, A. Magnetic, Durable, and Superhydrophobic Polyurethane@Fe₃O₄@SiO₂@fluoropolymer Sponges for Selective Oil Adsorption and Oil/Water Separation. *ACS Appl. Mater. Interfaces* **2015**, *7* (8), 4936–4946.
- (64) Gui, X.; Zeng, Z.; Lin, Z.; Gan, Q.; Xiang, R.; Zhu, Y.; Cao, A.; Tang, Z. Magnetic and Highly Recyclable Macroporous Carbon Nanotubes for Spilled Oil Sorption and Separation. *ACS Appl. Mater. Interfaces* **2013**, *5* (12), 5845–5850.
- (65) Yu, T.; Halouane, F.; Mathias, D.; Barras, A.; Wang, Z.; Lv, A.; Lu, S.; Xu, W.; Meziane, D.; Tiercelin, N.; Szunerits, S.; Boukherroub, R. Preparation of Magnetic, Superhydrophobic/Superoleophilic Polyurethane Sponge: Separation of Oil/Water Mixture and Demulsification. *Chem. Eng. J.* **2020**, *384*, 123339.
- (66) Zhang, X.; Wang, G.; Fu, F.; Gao, X.; Niu, F.; Wei, Q.; Hou, X. Recyclable Magnetically Driven Superhydrophobic Polyurethane Sponge for Highly Efficient Oil/Water Mixtures and Emulsions Separation. *IOP Conf. Ser. Earth Environ. Sci.* **2018**, *186* (4), 12032.
- (67) Liu, H.; Su, S.; Xie, J.; Ma, Y.; Tao, C. Preparation of Superhydrophobic Magnetic Stearic Acid Polyurethane Sponge for Oil-Water Separation. *J. Mater. Res.* **2020**, *35* (21), 2925–2935.
- (68) Bamonte, S.; Shubhashish, S.; Khanna, H.; Shuster, S.; Rubio, S. J. B.; Suib, S. L.; Alpay, S. P.; Sahoo, S. Magnetically Doped Molybdenum Disulfide Layers for Enhanced Carbon Dioxide Capture. *ACS Appl. Mater. Interfaces* **2022**, *14* (24), 27799–27813.
- (69) Shi, J.; Cui, H.; Xu, J.; Yan, N. Carbon Spheres Synthesized from KHCO₃ Activation of Glucose Derived Hydrochar with Excellent CO₂ Capture Capabilities at Both Low and High Pressures. *Sep. Purif. Technol.* **2022**, *294*, 121193.
- (70) Deville, S. Ice-Templating, Freeze Casting: Beyond Materials Processing. *J. Mater. Res.* **2013**, *28* (17), 2202.

Recommended by ACS

Accelerated Synthesis of Ordered Mesoporous Carbons Using Plasma

Anthony Griffin, Zhe Qiang, *et al.*

APRIL 17, 2023
ACS OMEGA

READ 

Recent Progress and Future Directions of Biomass-Derived Hierarchical Porous Carbon: Designing, Preparation, and Supercapacitor Applications

Yufeng Yin, Changyu Lu, *et al.*

FEBRUARY 15, 2023
ENERGY & FUELS

READ 

One-Step Acid-Induced Confined Conversion of Highly Oriented and Well-Defined Graphitized Cellulose Nanocrystals: Potential Advanced Energy Materials

Lumin Chen, Kam Chiu Tam, *et al.*

NOVEMBER 30, 2022
ACS SUSTAINABLE CHEMISTRY & ENGINEERING

READ 

Ultramicroporous Carbon Nanofibrous Mats for Hydrogen Storage

Alicia Vergara-Rubio, Silvia Goyanes, *et al.*

OCTOBER 19, 2022
ACS APPLIED NANO MATERIALS

READ 

Get More Suggestions >